Contact Geometry Selection in the Formation Process of a Single-Molecule Junction: Process Elucidation via Surface-Enhanced Raman Scattering Spectroscopy and *I–V* measurements

Moe Ichikawa,[1] *Kazuhito Tsukagoshi,*[2] *Tomoaki Nishino,*[1] *Satoshi Kaneko*[3]***

[1]*Department of Chemistry, School of Science, Institute of Science Tokyo, 2-12-1, Ookayama, Meguro-ku, Tokyo 152-8550, Japan.*

[2]*Research Center for Materials Nanoarchitectonics (MANA), National Institute for Materials Science (NIMS), 1-1 Tsukuba, Ibaraki 305-0044, Japan.*

[3]*Department of Materials Science and Engineering, School of Materials and Chemical Technology, Institute of Science Tokyo, 2-12-1, Ookayama, Meguro-ku, Tokyo 152-8550, Japan.*

KEYWORDS. Single-molecule junction, formation process, interface geometry, structure–property relationship, molecular electronics, surface-enhanced Raman scattering, current–voltage response, 1,4-phenylene diisocyanide

Abstract

A primary objective in the field of nanomaterials, especially nanoelectronic materials, is to precisely control the geometry of metal-molecule interfaces at the single-molecule level. This is because these interfaces significantly impact the physical properties of nanomaterials. Single-molecule junctions (SMJs) are a model system for studying the structure-property relationship at the single-molecule level because they are the basic units of metal-molecule-metal interfaces. Recently, unique and efficient properties have been observed in SMJs. Despite the beneficial and distinctive properties exhibited by SMJs, fabricating an SMJ with the desired structure remains a notable challenge. Herein, we demonstrate the selective fabrication of two conductive states based on a formation process. We focus on the Raman shift of the CN stretching mode in 1,4-phenylene diisocyanide (PDI)-semiconductor junction (SMJ) structures, as this shift sensitively reflects the contact geometry with which PDI bonds to the electrode. We study PDI SMJ formation during the breaking and making nanocontact. The breaking process produces a low-conductive state, and the making process generates a high-conductive state. Synchronized surface-enhanced Raman scattering and current–voltage measurements reveal the conductance-dependent Raman shift of the CN stretching mode. Density functional theory analysis of the vibrational shift shows that the parallel and tilted configurations correspond to the low- and high-conductive states, respectively, observed in the breaking and making processes. Rearrangement of the atomic configuration on the electrode surface affects the preferred junction configuration. Consequently, we can selectively fabricate two conductive states, as revealed by a spectroscopic technique. This contributes to precise control of the physical properties of nanoelectronic materials through fabrication of metal–molecule interface geometry at the single-molecule level. This development paves the way for reliable molecular electronics.

[Introduction]

The metal–molecule interface geometry is significant important for the development and improvement of nanomaterials.[1-8] The atomic configuration of heterogeneous catalysts has been demonstrated to affect reaction efficiencies,[7-8] and charge injection, governed by the metal–molecule interface, has been shown to considerably affect the performance of electronic materials, including organic semiconductors.[1-6] In essence, the precise regulation of the contact geometry at metal–molecule interfaces on a single-molecule basis has been demonstrated to markedly enhance the performance of nanomaterials.[7, 9-10] Single-molecule junctions (SMJs) have garnered considerable attention as a platform for exploring and elucidating the unique properties of nanomaterials at the single-molecule level.[11-13] Until now, unique physical property[14-19] or chemical reactions[13, 17-22] have been investigated using SMJs.[11-13] In order to evaluate physical properties or chemical reactions, it is essential to fabricate the desired contact geometry, such as an adsorption site or a molecular orientation. This is due to the fact that the contact geometry notably affects the electronic states of SMJs.[9, 13, 19] Although SMJs can be fabricated using different methods, typical methods are derived from two processes: the breaking[10, 13, 23] or making[13, 23-24] of a nanocontact.[11-13, 23] In previous studies, the dynamic geometric change induced in the formation of SMJs was studied by monitoring conductance as a function of the separation distance between the electrodes for the breaking and making processes.[9, 13, 23, 25] In the process of fracture, metal nanocontacts are subjected to persistent tensile forces. The thickness of the metal nanocontact undergoes a progressive decrease, ultimately resulting in the formation of a metal atomic contact. In this configuration, a single metal atom is connected to the protruded region of the electrodes, which is referred to as the "neck region."[26] The neck region is formed by extracting metal atoms from bulk electrodes through an external force, and its size is estimated to be 5–10 Å.[23, 26] The target molecule migrates to the atomic contact and bridges over the atomic contact, and an SMJ is formed after the rupture of the metal atomic contact.[23] Eventually, an SMJ ruptures under additional tensile tension, concomitant with the shrinkage of the neck region, which is referred to as snap back.[23, 26] Concurrently, as the electrodes approach one another, the capture of molecules on one side occurs at an optimal gap size. As the separation between the electrodes is reduced, a complete metal nanocontact is eventually established.[23, 26-27] The atomic configuration in which a molecule is connected to the electrodes differs from the formation process, *i.e.*, the presence of the neck region.[23, 26] This discrepancy suggests the hypothesis that distinct structures emerge during the processes of breaking and making. However, the effect of the formation process on the contact geometry remains ambiguous. The uncertainty surrounding the dependence of the formation process on the contact geometry hinders the sophistication of the SMJ fabrication process, which is essential for regulating the physical properties attributable to the contact geometry at the single-molecule level.

In this study, we present a novel methodology for the selective fabrication of the contact geometry of a 1,4-phenylene diisocyanide (PDI) SMJ formed during the breaking and making processes. This methodology employs a combination of current–voltage (I–V) response and surface-enhanced Raman scattering (SERS) measurements, which is a unique method for identifying the geometry of SMJs. In the nanogap, the strong electromagnetic field is enhanced, and the SERS signal is significantly amplified at atomic contact.[27-29] In SMJs, a strong SERS signal is attributed to the charge transfer triggered by the formation of SMJs, which enables the detection of vibrational modes in them.[30-33] The change in the Raman shift and fluctuation of the SERS intensity synchronized with the abrupt conductance change resulting from the formation of an SMJ enables the detection of the signal from SMJs.[30-34] A vibrational shift observed in their SERS spectra corresponds to changes in the contact geometry which is not fully investigated via conductance measurements alone.[30-31, 33] In particular, the vibrational peak originating from the CN stretching mode of PDI is considered a reliable marker because it is a prominent peak appearing around 2000 cm^{-1}. This peak is observed in an energy region that differs from the region where peaks attributed to the other functional groups appear, facilitating the clear identification of the CN stretching mode.[35-37] Moreover, the vibrational shift of the CN stretching mode is sensitive to the contact geometry where a molecule connects.[35-38] These spectroscopic advantages of PDI are expected to provide insights into the contact geometry at the single-molecule level.

Thus, in this study, we applied a combined SERS and *I*–*V* measurement system to a PDI SMJ. Initially, the conductive states of PDI SMJs were investigated based on conventional statistical conductance measurements[12, 25-26] during the breaking and making processes in the nanocontact. The results revealed a distinct low-conductive state (L state) and a broad high-conductive state (H state) in the breaking and making processes, respectively. In accordance with the definition of the conductive state, the combination of SERS with *I*–*V* measurements effectively detected the vibrational mode of PDI for the H and L states. A discernible shift was observed in the Raman shift of the CN stretching mode, which effectively distinguished the two states based on the Raman shift. The H state was characterized by a smaller Raman shift, whereas the L state exhibited a higher Raman shift. Compared with the spectra calculated based on density functional theory (DFT), PDI was bound to the atop site, with its molecular axis parallel to the junction configuration in the L state, while the tilted configuration was dominant for the H states. The degree of π back donation for the H state and that of σ donation for the L state, regulated by the contact geometry, play a crucial role in the Raman shift of the CN stretching mode. This shift allows for the detection of even minute changes in contact geometry. Consequently, SERS combined with the *I*–*V* measurements of PDI distinguished the contact geometry of PDI SMJ. Furthermore, the results demonstrated that the two conductive states could be selectively produced by choosing the appropriate formation process, which contributes to the precise control of the physical property of the nanoelectronic materials by the fabrication of the metal–molecule interface geometry at the single-molecule level. This development paves the way to the realization of reliable molecular electronics.

[Experimental section]

SMJs were fabricated using mechanically controllable break junction (MCBJ) technique. The electrode was fabricated on a phosphor bronze substrate using electron beam lithography and lift-off processes.[30-33, 39] Further details are presented in the Supporting Information Section S1.[9-12] Briefly, the MCBJ substrate was mounted in a three-point bending stage, comprising a stacked piezo element and two fixed counter supports (Figure 1(a)). A 3 mM tetrahydrofuran solution of PDI was deposited on the substrate and dried in air. The conductance of the Au nanocontact was monitored during the breaking and making processes of the nanocontact at a constant bias of 100 mV (Figure S1). During the breaking process, the Au nanocontact underwent gradual stretching through substrate bending, ultimately rupturing the Au nanocontact after SMJ formation (Figure 1(a)). During the making process, the two separated electrodes were brought closer through the restoring force of the substrate, ultimately connecting the Au nanocontact after SMJ formation (Figure 1(d)). The substrate was repeatedly bent and unbent in a controlled manner to facilitate the making and breaking of the nanocontact, allowing statistical analysis of the conductance value during the making and breaking process. The SERS spectra of PDI SMJ were measured using a conventional Raman system (Nanofinder 30A, Tokyo Instruments, Japan). The wavelength and intensity of excitation energy were 785 nm and 4.4 mW, respectively. The SERS spectra were acquired every 1 s. When the conductance under consideration was obtained, the movement of the piezo was halted. The SERS spectra and conductance were simultaneously measured. The detailed measurement protocol is provided in the Supporting Information—Sections S1 and S2.

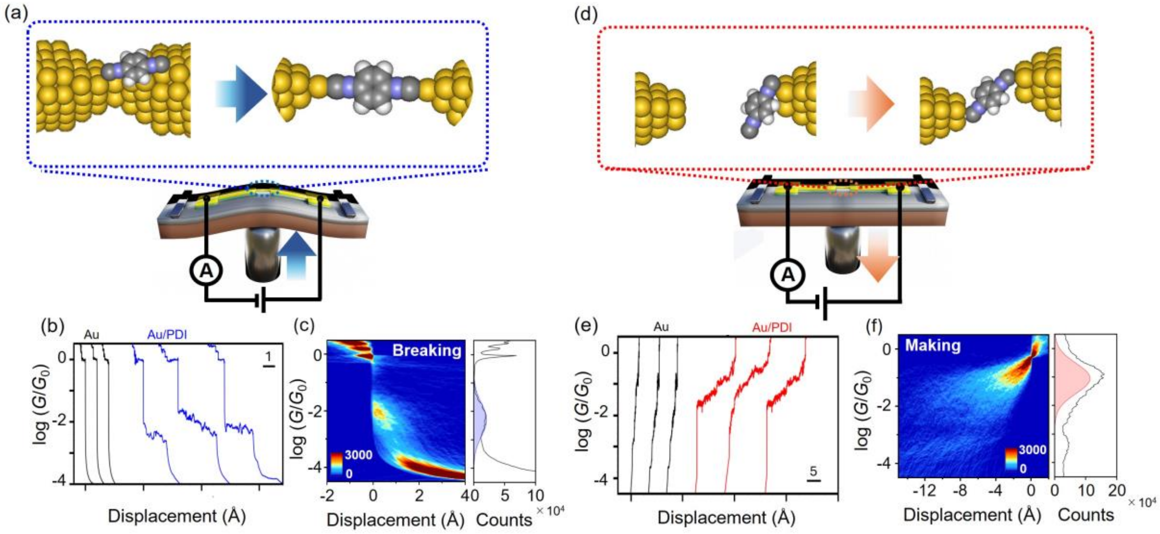

Figure 1. Conductance measurements of SMJs using MCBJ technique. (a, d) Schematic of SMJ formation during the (a) breaking and (d) making processes. (b, e) Conductance traces for the (b) breaking and (e) making processes. Black and colored lines represent the trace of the Au contact without and with PDI. Bias was 100 mV. (c, f) 2D and 1D conductance histograms for the (c) breaking and (f) making processes.

Theoretical calculations began by building a geometric model of the contact geometry (details are presented in Supporting Information Section S3). The pyramidal Au tip was fabricated using a stacked Au (111) surface and attached to PDI via an adsorption structure. The contact geometry was fabricated as a function of the separation distance between the two electrodes. The contact geometry at the separation distance that yielded the local energy minimum was optimized using DFT with B3PW91 functional. The basis functions were LanL2DZ for Au and 6-31 G (d, p) for carbon, hydrogen, and nitrogen atoms. The Raman shift of the PDI junction was calculated using Gaussian 16 after geometric optimization.

[Results and Discussion]

First, we investigated the conductance properties during the breaking and making processes of the nanocontact. In the breaking process, conductance traces obtained with a clean Au electrode showed clear plateaus around 1 G_0 ($G_0 = 2e^2/h$, where e and h denote elementary charge and the Planck constant, respectively) due to the formation of metal atomic contacts (black curves in Figure 1(b), Figure S2 in the Supporting Information Section S2).[26] In contrast, in the presence of PDI, additional plateaus below 1 G_0 appeared (blue curves in Figure 1(b)), indicating the formation of PDI SMJs after the rupture of metal atomic contacts. The two-dimensional (2D) conductance histogram in Figure 1(c), constructed by superimposing 1249 conductance traces, showed a distinct state at 10^{-2} G_0, which was comparable to previously reported conductance for PDI.[40] In the making process, conductivity gradually increased, exhibiting small plateaus for clean Au electrodes (black curves in Figure 1(e), Figure S2); however, a distinct plateau around 10^{-1} G_0 was observed in the presence of PDI (red curves in Figure 1(e)). The corresponding 1D and 2D conductance histograms, constructed by superimposing 1199 conductance traces, demonstrated prominent peaks or states around 10^{-1} G_0 (Figure 1(f)). The small satellite peak around 10^{-3} G_0 was attributed to a junction of a dimer or oligomers.[40] To define the conductance region, the 1D histogram was fitted by the gaussian function. The conductance of the L state was $10^{-2.3(\pm 0.7)}$ G_0, and that of the H state was $10^{-1.1(\pm 0.6)}$ G_0. Conductance measurements clearly showed that the preferred conductance state differed depending on the SMJ formation process.

To clarify the contact geometry of each conductive state, the SERS and I–V curves were measured in the two states, which are defined by fitting the 1D conductance histogram. It was observed that the effect of the external bias on the contact geometry was negligible (Supporting Information Fig. S7). Figures 2(a) and (b) illustrate the time course of conductance (Figure 2(a)) and SERS intensity (Figure 2(b)) for PDI SMJ in the L state (another example is displayed in Figure S6 in Supporting Information Section S4). During measurements, the conductive state kept 10^{-2} G_0, and the vibrational modes attributed to PDI were observed. The intensity modulation of the peaks or change in the Raman shift originated from the geometry change at the contact.[41-43] It is noticeable that the fluctuation of the SERS intensity is correlated with the fluctuation of the conductance. Figure 2(c) shows the spectra of the H and L states. Both states exhibited typical vibrational modes, such as the CH bending (δ_{CH}), C=C stretching (υ_{CC}), and C≡N stretching (υ_{CN}), which were observed at 1171, 1601, and 2124 cm^{-1} in the spectra of PDI powder measured as the reference sample marked as triangle in Figure 2(c).[36, 44-46] Another examples and histogram of the Raman shift are displayed in Figures S7 and S8. The detailed assignment for the peaks is presented in Table S1 (Supporting Information Section S5). For the H state, the Raman shift of the CN stretching mode, observed at 2067 cm^{-1}, was smaller than that for the reference powder sample (2124 cm^{-1}). In contrast, the Raman shift of the CN stretching mode for the L state was observed at 2200 cm^{-1}, was higher than that for the reference powder sample. The difference in the Raman shifts between the H and L states was 133 cm^{-1}, indicating that the CN stretching mode served as a marker of conducting states. The significant change in the Raman shift for the CN stretching mode was due to a change in the electron density of the CN induced by electron transfer between PDI and the Au electrode,[36-37] as discussed in the following section.

The relationship between the Raman shift of the CN stretching mode and conductance was investigated by measuring the *I*–*V* and SERS spectra for 39 distinct trials, amounting to 1252 spectra in total, which allows statical analysis in the conductance region determined by the break

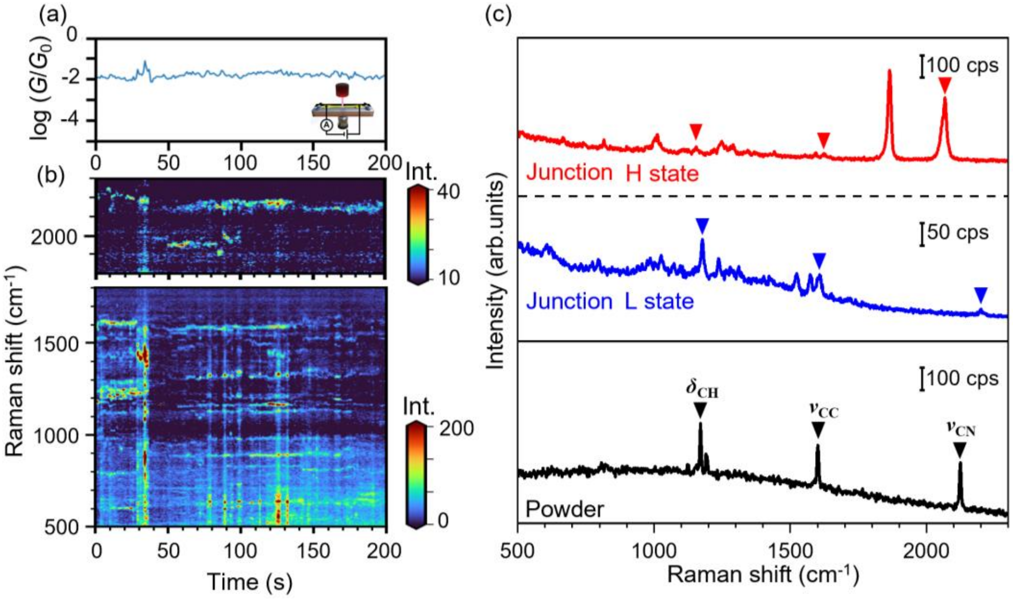

Figure 2. (a, b) Synchronized SERS and conductance measurements. (a) Time course of conductance during SERS measurement. Bias voltage: 100 mV. A schematic image for the experimental measurement system is shown in inset. (b) The example of the time courses of SERS and conductance. (c) The SERS spectrum for SMJs observed at a conductance of 60 mG_0 (top panel; red curve) and 13 mG_0 (middle panel; blue curve), along with the Raman spectrum of the PDI powder sample (bottom panel; black curve).

junction measurement in the previous paragraph. Figure 3(a) shows correlations among conductance, Raman shift, and SERS intensity. The SERS intensities and Raman shifts were estimated through the automatic fitting of the SERS spectra with the Lorentz function (Figure S1 in the Supporting Information S1).[22, 30, 47] At the horizontal dotted line is the border of the H and L states which is defined by the conductance histogram. The vertical dotted line is the Raman shift of the CN stretching mode of the powder sample. The tendency of the Raman shift of the CN stretching mode was consistent with that observed in Figure 2(c). The Raman shift of the H state was smaller than that of the powder sample; furthermore, the Raman shift observed in the L state showed an opposite tendency to that noticed in the H state. In addition, the SERS intensity of the CN stretching mode was higher in the H state than in the L state. Although the tendency was also observed in another vibrational mode (Figure S10 in Supporting Information section S6), the Raman shifts of the CN stretching mode were more significant because the carbon atom is directly bonded to the electrode surface, as we mentioned in the previous section. Therefore, the correlation between conductance and Raman shift indicates that the conductive states observed in the breaking and making processes are due to the different geometry of the SMJs, which induces the difference in Raman shift of the CN stretching mode.

To elucidate the geometry change depending on Raman shift, five geometrical models with different adsorption sites or orientations were considered using DFT (Figures S3 in Supporting Information Section S3), which covers possible atomic configurations in the PDI junction. Since thermodynamically stable states predominantly contribute to the SERS spectrum, we revealed the geometry with a local energy minimum for each geometry by modulating the separation distance (Figure S4, S5 in Supporting Information Section S3). The results revealed that the contact geometry in which PDI was connected via the atop site of the electrode was thermodynamically preferable among all geometries considered, which was consistent with previous studies (Supporting Information Section S3).[36, 48] In the case of nitrogen protonation, the SERS spectra are significantly different from the case of the other geometric changes. The peak of the CN stretching mode could not be observed in the region of 1800-2000 cm^{-1} (Figure S7), indicating that the observed change in the Raman shift of the CN stretching mode is due to the contact geometry. The calculated spectra showed that when PDI adopted a tilted configuration, the CN stretching mode had smaller Raman shift. In contrast, when PDI took a parallel configuration, the CN stretching mode exhibited higher Raman shift (Figure 3(b)). The calculated spectra of all models are shown in Figure S9 in the Supporting Information Section S5. The calculated trend of the Raman shift of the CN stretching mode indicates that the L state observed in the breaking process is derived from a parallel configuration, while the H state observed in the making process is derived from a tilted configuration. It is noteworthy that the effect of the dynamic motion of the Au atoms can be observed in the low-frequency region of ca. 100 cm^{-1}, which is different from the Raman shift of the CN stretching mode.[49-50] Moreover, conductance dependence of the Raman shift of the CN stretching mode observed in Figure 3(a) agreed well with the separation distance dependence of the conductivity, supporting the geometry assessment mentioned above.[31, 33, 51-52] In the tilted configuration, the π–electrode interaction contributed more effectively to electron transport, increasing conductivity, which is typical of aromatic molecules bonded to a metal electrodes.[31, 33, 51-52] In contrast, conductivity was reduced in the parallel configuration because the π orbital was orthogonal to the Au–CN bond. [31, 33, 51-52]

The geometry dependence of Raman shift could be predominantly interpreted in terms of electron transfer between PDI and the Au electrodes. A detailed discussion is provided in Supporting Information Sections S7 and S8. The bonding states of PDI SMJ comprised the d–π* and d–σ states created by σ donation and π back donation (Figure S11).[37, 53] In the parallel configuration, the lone pair of PDI, which had an antibonding character of the CN bond,

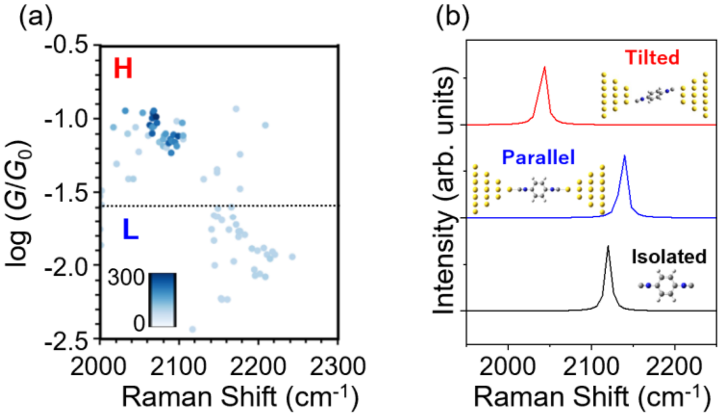

Figure 3. (a) Correlation histogram for the conductance and vibrational energy of the CN stretching mode. Histogram was constructed from 1252 spectra obtained from 39 distinct trials. Color intensity represents the average SERS intensity in a bin size of 1 cm^{-1} × 0.001. Vertical dotted line represents the vibrational energy of the CN stretching mode for the powder sample. Horizontal dotted line denotes the limit of the conductance of the L state estimated by the full width at half maximum of the Gaussian function described in Figure 1(c). (b) The calculated PDI spectra with the CN stretching mode. Red curve represents the tilted configuration, blue curve denotes PDI SMJ with the parallel configuration, and black curve indicates an isolated PDI molecule.

dominantly interacted with the d states of Au via σ donation, forming the d–σ state.[37, 53-54] Electron transfer from PDI to Au reduced the electron density of the antibonding states of CN, strengthening the CN bond via σ donation and thus increasing the Raman shift of the CN stretching mode. Meanwhile, in the tilted configuration, the π* state more contributes to bonding states than that in the parallel configuration, and electron transfer from the electronic state of Au to the unoccupied π* state of PDI enhanced via π back donation. The weakened CN bonds via π back donation decreases the vibrational energy of the CN stretching modes.[30-31] Consequently, the Raman shift of the CN stretching mode of the H state diminished and that of the L state increased. Minute geometry changes modulated the degree of electron transfer, which affected the observed Raman shift in each conductive state. The decrease in electron transfer induced by the stretching of the Au–C bond leads to a decrease in the vibrational energy of the CN stretching mode, as shown in Figure S12. On the other hand, the increase in the interaction between PDI and electrodes induced by the tilting leads to a decrease in the vibrational energy of the CN stretching mode as shown in Fig. S13, as discussed in Supporting Information section S8.

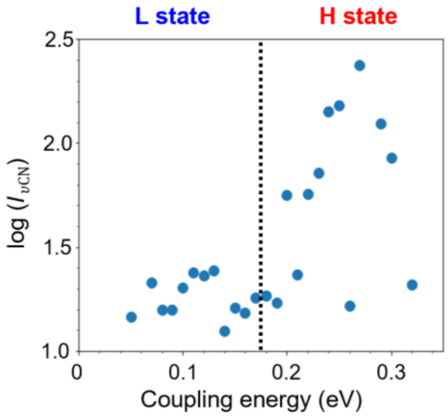

Figure 4. Coupling energy (Γ) dependency of SERS intensity. SERS intensity was averaged every 0.01 eV. Vertical dotted line represents the border between the H and L state.

The SERS intensity of the CN stretching mode as a function of the conductive states was discussed in terms of the charge-transfer effects in SERS signal enhancement. The coupling energy between the molecular orbital and metal electronic states was estimated by analyzing the *I–V* curves observed synchronously with SERS measurements. The *I–V* curves were fitted using the Landauer and the Breit–Wigner formula,[33, 55] which estimated the coupling energy between the PDI molecular orbital and Au electronic states (Figure S14 in Supporting Information Section S9). Figure 4 shows the relationship between the coupling energy and SERS intensity of the CN stretching mode. The border at the L and H states was estimated by the relationship between conductance and coupling energy (details are provided in Supporting Information Section S9). The SERS intensity increased with increasing coupling energy, which was attributed to the enhancement of charge-transfer resonance.[31, 33] The other possibility for enhancing SERS intensity is the locally enhanced electromagnetic field at the atomically protruding electrodes.[56-58] At the atomically protruding electrodes, such as metal adatoms, the confined optical field is localized to the pico-sized space, resulting in extreme field gradients.[56-58] The additional contact with the protuberance increases the SERS intensity and the coupling. In fact, in the H state geometry, the molecule has more atomic contact with the surface, which is consistent with the geometry where the PDI π surface connects to the metal surface, although the exact atomic configuration of the Au surface still remains unclear. Therefore, this increase in SERS intensity was consistent with the conclusion that PDI was tilted in the H state, while it was in a parallel state in the L states.

Finally, the preferred contact geometry depending on the formation process of SMJs was discussed. As discussed above, synchronized measurements of SERS and *I–V* revealed that the parallel configuration was dominant in the breaking process. In contrast, the tilted configuration was dominant in the making process, which was reasonable considering the dynamic motion of the electrode atoms.[40] In the breaking process, PDI tended to be connected via the atop site at the apex of the protruded neck region on the electrode due to tensile tension.[40] The strong σ bond between CN and Au atoms facilitated parallel configuration formation in the breaking process. Upon bond breakage, atoms comprising the neck region immediately shrunk via snap back.[23, 26] During the making process, PDI adhered via the π–electrode interaction in a tilted configuration to a flat surface that emerged following snap back. This selectivity of the geometry depending on the formation process is due to a non-reversible geometrical change rather than a reversible one owing to the snap back. In fact, the selectivity is considered to be based on kinetic control rather than thermodynamic control. The presence of metastable states with minute geometry differences, such as varying adsorption sites, could be observed in the H state. This is discussed in more detail in Supporting Information Sections S5 and S8. Therefore, the H state exhibited a broad distribution of conductance in the conductance histogram. Conversely, the geometry configuration was constrained in the L state because possible bonding site is limited to the atop site due to the strong σ-donation, resulting in a narrow distribution in the conductance histogram, as discussed in Supporting Section S8.

[Conclusion]

In conclusion, the present study demonstrated the selective fabrication of SMJs via the formation process, which was elucidated by a combination of I–V and SERS measurements. A thorough statistical analysis of the breaking and making processes revealed a significant discrepancy. The L state was only observed during the breaking process, while the H state was predominant during the making process. Synchronized conductance and SERS measurements revealed a prominent change in the Raman shift in the CN stretching mode between the H and L states. A subsequent analysis of the SERS spectra using DFT calculation enabled the geometry assignment of the H and L states. The L state demonstrated the parallel configuration, while the H state exhibited the tilted configuration via the π–electrode interaction. This finding suggests that the preferred geometry is contingent upon the formation process, with the contact geometry being determined by the atomic configuration of the electrode during the formation process. This indicates that the SMJ structure can be controlled by the formation process. The findings of this study contributed to the control of the contact geometry of the metal–molecule interface, paving the way to regulate the precise physical properties of the nanoelectronic materials, such as molecular devices.

ASSOCIATED CONTENT

Supporting Information. The supporting information is available free of charge at https://pubs.acs.org/journal/aanmf6.

Fabrication of the electrodes and measurement protocol, Conductance measurements for clean Au nanocontact, Modeling for the theoretical calculations for the Raman shift, Time course of the SERS intensity and conductance, SERS spectra of the PDI SMJ and assignment for the vibrational modes, Geometrical dependence of the SERS spectra of the PDI-SMJ, The bonding states in a PDI SMJ, Vibrational shift of the CN stretching mode induced by the minute geometry change, and Current-voltage response in a SMJ (PDF)

AUTHOR INFORMATION

Corresponding Author

***Satoshi Kaneko** *Department of Chemical Science and Engineering, School of Materials and Technology, Institute of Science Tokyo, 2-12-1. Ookayama, Meguro-ku, Tokyo 152-8550, Japan; orcid.org/0000-0002-0351-6681;* Email: kaneko.s@mct.isct.ac.jp

Authors

Moe Ichikawa *Department of Chemistry, School of Science, Institute of Science Tokyo, 2-12-1, Ookayama, Meguro-ku, Tokyo 152-8550, Japan.*

Kazuhito Tsukagoshi *Research Center for Materials Nanoarchitectonics (MANA), National Institute for Materials Science (NIMS), 1-1 Tsukuba, Ibaraki 305-0044, Japan; orcid.org/0000-0001-9710-2692.*

Tomoaki Nishino *Department of Chemistry, School of Science, Institute of Science Tokyo, 2-12-1, Ookayama, Meguro-ku, Tokyo 152-8550, Japan; orcid.org/0000-0002-6691-583.*

Author Contributions

The manuscript was written through contributions of all authors. All authors have given approval to the final version of the manuscript.

Funding Sources

Grants-in-Aid for Scientific Research (No. 20K05445, 22H04974) from MEXT, Japan.

Research granted from Murata Science and Education Foundation

Research granted from The Hattori Hokokai Foundation.

Notes

The authors declare no competing financial interest.

ACKNOWLEDGMENT

The numerical calculations were performed on a TSUBAME 4.0 supercomputer at Institute of Science Tokyo. This work was partially supported by a Grant-in-Aid for Scientific Research (20K05445, 22H04974), research granted from Murata Science and Education Foundation, and Research granted from The Hattori Hokokai Foundation.

REFERENCES

(1) Fahlman, M.; Fabiano, S.; Gueskine, V.; Simon, D.; Berggren, M.; Crispin, X., Interfaces in organic electronics. *Nat. Rev. Mater.* **2019,** *4*, 627-650.
(2) Chen, Y.; Tamblyn, I.; Quek, S. Y., Energy level alignment at hybridized organic–metal interfaces: The role of many-electron effects. *J. Phys. Chem. C* **2017,** *121*, 13125-13134.
(3) Lin, C. C.; Yang, K. D.; Shih, M. C.; Huang, S. K.; Chen, T. P.; Hsu, H. C.; Chuang, C. A.; Huang, C. Y.; Wang, L.; Chen, C. C.; Ho, C. H.; Chiu, Y. P.; Chen, C. W., Internal built-in electric fields at organic-inorganic interfaces of two-dimensional ruddlesden-popper perovskite single crystals. *ACS Appl. Mater. Interfaces* **2022,** *14*, 19818-19825.
(4) Tarakeshwar, P.; Palma, J. L.; Holland, G. P.; Fromme, P.; Yarger, J. L.; Mujica, V., Probing the nature of charge transfer at nano-bio interfaces: Peptides on metal oxide nanoparticles. *J. Phys. Chem. Lett.* **2014,** *5*, 3555-3559.
(5) Li, P.; Lu, Z.-H., Interface engineering in organic electronics: Energy-level alignment and charge transport. *Small Sci.* **2020,** *1*, 2000015.
(6) Zhu, X. Y., Charge transport at metal−molecule interfaces: A spectroscopic view. *J. Phys. Chem. B* **2004,** *108*, 8778-8793.
(7) Ouyang, M.; Papanikolaou, K. G.; Boubnov, A.; Hoffman, A. S.; Giannakakis, G.; Bare, S. R.; Stamatakis, M.; Flytzani-Stephanopoulos, M.; Sykes, E. C. H., Directing reaction pathways via in situ control of active site geometries in PdAu single-atom alloy catalysts. *Nat. Commun.* **2021,** *12*, 1549.
(8) Sun, G.; Zhao, Z. J.; Mu, R.; Zha, S.; Li, L.; Chen, S.; Zang, K.; Luo, J.; Li, Z.; Purdy, S. C.; Kropf, A. J.; Miller, J. T.; Zeng, L.; Gong, J., Breaking the scaling relationship via thermally stable Pt/Cu single atom alloys for catalytic dehydrogenation. *Nat. Commun.* **2018,** *9*, 4454.
(9) Chen, L.; Yang, Z.; Lin, Q.; Li, X.; Bai, J.; Hong, W., Evolution of single-molecule electronic interfaces. *Langmuir* **2024,** *40*, 1988-2004.
(10) Xu, B.; Tao, N. J., Measurement of single-molecule resistance by repeated formation of molecular junctions. *Science* **2003,** *301*, 1221-1223.
(11) Xie, X.; Li, P.; Xu, Y.; Zhou, L.; Yan, Y.; Xie, L.; Jia, C.; Guo, X., Single-molecule junction: A reliable platform for monitoring molecular physical and chemical processes. *ACS Nano* **2022,** *16*, 3476-3505.
(12) Evers, F.; Korytár, R.; Tewari, S.; van Ruitenbeek, J. M., Advances and challenges in single-molecule electron transport. *Rev. Mod. Phys.* **2020,** *92*, 035001.
(13) Gorenskaia, E.; Low, P. J., Methods for the analysis, interpretation, and prediction of single-molecule junction conductance behaviour. *Chem. Sci.* **2024,** *15*, 9510-9556.

(14) Thomas, J. O.; Limburg, B.; Sowa, J. K.; Willick, K.; Baugh, J.; Briggs, G. A. D.; Gauger, E. M.; Anderson, H. L.; Mol, J. A., Understanding resonant charge transport through weakly coupled single-molecule junctions. *Nat. Commun.* **2019,** *10*, 4628.

(15) Park, J.; Pasupathy, A. N.; Goldsmith, J. I.; Chang, C.; Yaish, Y.; Petta, J. R.; Rinkoski, M.; Sethna, J. P.; Abruna, H. D.; McEuen, P. L.; Ralph, D. C., Coulomb blockade and the kondo effect in single-atom transistors. *Nature* **2002,** *417*, 722-725.

(16) Liu, J.; Huang, X.; Wang, F.; Hong, W., Quantum interference effects in charge transport through single-molecule junctions: Detection, manipulation, and application. *Acc. Chem. Res.* **2019,** *52*, 151-160.

(17) Chen, Z.; Grace, I. M.; Woltering, S. L.; Chen, L.; Gee, A.; Baugh, J.; Briggs, G. A. D.; Bogani, L.; Mol, J. A.; Lambert, C. J.; Anderson, H. L.; Thomas, J. O., Quantum interference enhances the performance of single-molecule transistors. *Nat. Nanotechnol.* **2024,** *19*, 986-992.

(18) Mitchell, A. K.; Pedersen, K. G. L.; Hedegard, P.; Paaske, J., Kondo blockade due to quantum interference in single-molecule junctions. *Nat. Commun.* **2017,** *8*, 15210.

(19) Li, T.; Bandari, V. K.; Schmidt, O. G., Molecular electronics: Creating and bridging molecular junctions and promoting its commercialization. *Adv. Mater.* **2023,** *35*, e2209088.

(20) Jia, C.; Wang, J.; Yao, C.; Cao, Y.; Zhong, Y.; Liu, Z.; Liu, Z.; Guo, X., Conductance switching and mechanisms in single-molecule junctions. *Angew. Chem. Int. Ed. Engl.* **2013,** *52*, 8666-8670.

(21) Roldan, D.; Kaliginedi, V.; Cobo, S.; Kolivoska, V.; Bucher, C.; Hong, W.; Royal, G.; Wandlowski, T., Charge transport in photoswitchable dimethyldihydropyrene-type single-molecule junctions. *J. Am. Chem. Soc.* **2013,** *135*, 5974-5977.

(22) Kobayashi, S.; Kaneko, S.; Tamaki, T.; Kiguchi, M.; Tsukagoshi, K.; Terao, J.; Nishino, T., Principal component analysis of surface-enhanced raman scattering spectra revealing isomer-dependent electron transport in spiropyran molecular junctions: Implications for nanoscale molecular electronics. *ACS Omega* **2022,** *7*, 5578-5583.

(23) Fu, T.; Frommer, K.; Nuckolls, C.; Venkataraman, L., Single-molecule junction formation in break-junction measurements. *J. Phys. Chem. Lett.* **2021,** *12*, 10802-10807.

(24) van Zalinge, H.; Schiffrin, D. J.; Bates, A. D.; Haiss, W.; Ulstrup, J.; Nichols, R. J., Single-molecule conductance measurements of single- and double-stranded DNA oligonucleotides. *ChemPhysChem* **2006,** *7*, 94-98.

(25) Kamenetska, M.; Koentopp, M.; Whalley, A. C.; Park, Y. S.; Steigerwald, M. L.; Nuckolls, C.; Hybertsen, M. S.; Venkataraman, L., Formation and evolution of single-molecule junctions. *Phys. Rev. Lett.* **2009,** *102*, 126803.

(26) Yanson, A. I.; Bollinger, G. R.; van den Brom, H. E.; Agraït, N.; van Ruitenbeek, J. M., Formation and manipulation of a metallic wire of single gold atoms. *Nature* **1998,** *395*, 783-785.

(27) Liu, Z.; Ding, S. Y.; Chen, Z. B.; Wang, X.; Tian, J. H.; Anema, J. R.; Zhou, X. S.; Wu, D. Y.; Mao, B. W.; Xu, X.; Ren, B.; Tian, Z. Q., Revealing the molecular structure of single-molecule junctions in different conductance states by fishing-mode tip-enhanced raman spectroscopy. *Nat. Commun.* **2011,** *2*, 305.

(28) Liu, S.; Hammud, A.; Wolf, M.; Kumagai, T., Atomic point contact raman spectroscopy of a Si(111)-7 x 7 surface. *Nano Lett.* **2021,** *21*, 4057-4061.

(29) Park, Y.; Hamada, I.; Hammud, A.; Kumagai, T.; Wolf, M.; Shiotari, A., Atomic-precision control of plasmon-induced single-molecule switching in a metal-semiconductor nanojunction. *Nat. Commun.* **2024,** *15*, 6709.

(30) Homma, K.; Kaneko, S.; Tsukagoshi, K.; Nishino, T., Intermolecular and electrode-molecule bonding in a single dimer junction of naphthalenethiol as revealed by surface-enhanced Raman scattering combined with transport measurements. *J. Am. Chem. Soc.* **2023,** *145*, 15788-15795.

(31) Kobayashi, S.; Kaneko, S.; Kiguchi, M.; Tsukagoshi, K.; Nishino, T., Tolerance to stretching in thiol-terminated single-molecule junctions characterized by surface-enhanced raman scattering. *J. Phys. Chem. Lett.* **2020,** *11*, 6712-6717.

(32) Yasuraoka, K.; Kaneko, S.; Fujii, S.; Nishino, T.; Tsukagoshi, K.; Juhasz, G.; Kiguchi, M., Effect of bias voltage on a single-molecule junction investigated by surface-enhanced Raman scattering. *J. Phys. Chem. C* **2019,** *123*, 15267-15272.

(33) Kaneko, S.; Murai, D.; Marques-Gonzalez, S.; Nakamura, H.; Komoto, Y.; Fujii, S.; Nishino, T.; Ikeda, K.; Tsukagoshi, K.; Kiguchi, M., Site-selection in single-molecule junction for highly reproducible molecular electronics. *J. Am. Chem. Soc.* **2016,** *138*, 1294-1300.

(34) Kaneko, S.; Montes, E.; Suzuki, S.; Fujii, S.; Nishino, T.; Tsukagoshi, K.; Ikeda, K.; Kano, H.; Nakamura, H.; Vazquez, H.; Kiguchi, M., Identifying the molecular adsorption site of a single molecule junction through combined Raman and conductance studies. *Chem. Sci.* **2019,** *10*, 6261-6269.

(35) Yamakoshi, H.; Dodo, K.; Palonpon, A.; Ando, J.; Fujita, K.; Kawata, S.; Sodeoka, M., Alkyne-tag Raman imaging for visualization of mobile small molecules in live cells. *J. Am. Chem. Soc.* **2012,** *134*, 20681-20689.

(36) Hu, J.; Tanabe, M.; Sato, J.; Uosaki, K.; Ikeda, K., Effects of atomic geometry and electronic structure of platinum surfaces on molecular adsorbates studied by gap-mode sers. *J. Am. Chem. Soc.* **2014,** *136*, 10299-102307.

(37) Ikeda, K.; Fujimoto, N.; Uehara, H.; Uosaki, K., Raman scattering of aryl isocyanide monolayers on atomically flat Au(1 1 1) single crystal surfaces enhanced by gap-mode plasmon excitation. *Chem. Phys. Lett.* **2008,** *460*, 205-208.

(38) Hu, S.; Liu, B. J.; Feng, J. M.; Zong, C.; Lin, K. Q.; Wang, X.; Wu, D. Y.; Ren, B., Quantifying surface temperature of thermoplasmonic nanostructures. *J. Am. Chem. Soc.* **2018,** *140*, 13680-13686.

(39) Martin, C. A.; Ding, D.; van der Zant, H. S. J.; van Ruitenbeek, J. M., Lithographic mechanical break junctions for single-molecule measurements in vacuum: Possibilities and limitations. *New J. Phys.* **2008,** *10*, 065008.

(40) Vladyka, A.; Perrin, M. L.; Overbeck, J.; Ferradas, R. R.; Garcia-Suarez, V.; Gantenbein, M.; Brunner, J.; Mayor, M.; Ferrer, J.; Calame, M., In-situ formation of one-dimensional coordination polymers in molecular junctions. *Nat. Commun.* **2019,** *10*, 262.

(41) Jakob, L. A.; Deacon, W. M.; Zhang, Y.; de Nijs, B.; Pavlenko, E.; Hu, S.; Carnegie, C.; Neuman, T.; Esteban, R.; Aizpurua, J.; Baumberg, J. J., Giant optomechanical spring effect in plasmonic nano- and picocavities probed by surface-enhanced raman scattering. *Nat. Commun.* **2023,** *14*, 3291.

(42) Kos, D.; Di Martino, G.; Boehmke, A.; de Nijs, B.; Berta, D.; Foldes, T.; Sangtarash, S.; Rosta, E.; Sadeghi, H.; Baumberg, J. J., Optical probes of molecules as nano-mechanical switches. *Nat. Commun.* **2020,** *11*, 5905.

(43) Yasuraoka, K.; Kaneko, S.; Kobayashi, S.; Tsukagoshi, K.; Nishino, T., Surface-enhanced raman scattering stimulated by strong metal-molecule interactions in a C_{60} single-molecule junction. *ACS Appl. Mater. Interfaces* **2021,** *13*, 51602-51607.

(44) Bae, S. J.; Lee, C.-R.; Choi, I. S.; Hwang, C.-S.; Gong, M.-S.; Kim, K.; Joo, S.-W., Adsorption of 4-biphenylisocyanide on gold and silver nanoparticle surfaces: Surface-enhanced raman scattering study. *J. Phys. Chem. B* **2002,** *106*, 7076-7080.

(45) Ahn, J.; Shi, S.; Vannatter, B.; Qin, D., Comparative study of the adsorption of thiol and isocyanide molecules on a silver surface by in situ surface-enhanced Raman scattering. *J. Phys. Chem. C* **2019,** *123*, 21571-21580.

(46) Sato, S.; Iwase, S.; Namba, K.; Ono, T.; Hara, K.; Fukuoka, A.; Uosaki, K.; Ikeda, K., Electrical matching at metal/molecule contacts for efficient heterogeneous charge transfer. *ACS Nano* **2018,** *12*, 1228-1235.

(47) Sadezky, A.; Muckenhuber, H.; Grothe, H.; Niessner, R.; Pöschl, U., Raman microspectroscopy of soot and related carbonaceous materials: Spectral analysis and structural information. *Carbon* **2005,** *43*, 1731-1742.

(48) Li, Y.; Lu, D.; Swanson, S. A.; Scott, J. C.; Galli, G., Microscopic characterization of the interface between aromatic isocyanides and Au(111): A first-principles investigation. *J. Phys. Chem. C* **2008,** *112*, 6413-6421.

(49) Cates, M.; Miller, D. R., Measurement of Au(111) surface phonons by low energy helium scattering. *J. Electron. Spectrosc. Relat. Phenom.* **1983,** *30*, 157-162.
(50) Guo, Y.; Adessi, C.; Cobian, M.; Merabia, S., Atomistic simulation of phonon heat transport across metallic vacuum nanogaps. *Phys. Rev. B* **2022,** *106*, 085403.
(51) Quek, S. Y.; Kamenetska, M.; Steigerwald, M. L.; Choi, H. J.; Louie, S. G.; Hybertsen, M. S.; Neaton, J. B.; Venkataraman, L., Mechanically controlled binary conductance switching of a single-molecule junction. *Nat. Nanotechnol.* **2009,** *4*, 230-234.
(52) Diez-Perez, I.; Hihath, J.; Hines, T.; Wang, Z. S.; Zhou, G.; Mullen, K.; Tao, N., Controlling single-molecule conductance through lateral coupling of pi orbitals. *Nat. Nanotechnol.* **2011,** *6*, 226-231.
(53) Ikeda, K.; Fujimoto, N.; Uosaki, K., Nanoscale optical and mechanical manipulation of molecular alignment in metal–molecule–metal structures. *J. Phys. Chem. C* **2014,** *118*, 21550-21557.
(54) Kim, N. H.; Kim, K., Adsorption characteristics of arylisocyanide on Au and Pt electrode surfaces: Surface-enhanced raman scattering study. *J. Phys. Chem. B* **2006,** *110*, 1837-1842.
(55) Kim, Y.; Pietsch, T.; Erbe, A.; Belzig, W.; Scheer, E., Benzenedithiol: A broad-range single-channel molecular conductor. *Nano Lett.* **2011,** *11*, 3734-3738.
(56) Griffiths, J.; Foldes, T.; de Nijs, B.; Chikkaraddy, R.; Wright, D.; Deacon, W. M.; Berta, D.; Readman, C.; Grys, D. B.; Rosta, E.; Baumberg, J. J., Resolving sub-angstrom ambient motion through reconstruction from vibrational spectra. *Nat. Commun.* **2021,** *12*, 6759.
(57) Carnegie, C.; Griffiths, J.; de Nijs, B.; Readman, C.; Chikkaraddy, R.; Deacon, W. M.; Zhang, Y.; Szabo, I.; Rosta, E.; Aizpurua, J.; Baumberg, J. J., Room-temperature optical picocavities below 1 nm^3 accessing single-atom geometries. *J. Phys. Chem. Lett.* **2018,** *9*, 7146-7151.
(58) Benz, F.; Schmidt, M. K.; Dreismann, A.; Chikkaraddy, R.; Zhang, Y.; Demetriadou, A.; Carnegie, C.; Ohadi, H.; de Nijs, B.; Esteban, R.; Aizpurua, J.; Baumberg, J. J., Single-molecule optomechanics in "picocavities". *Science* **2016,** *354*, 726-729.